ACS Partner Journal

CHEMICAL & BIOMEDICAL IMAGING

pubs.acs.org/ChemBioImaging

Article

Quantitative Assessment of Pulmonary Fibrosis in a Murine Model via a Multimodal Imaging Workflow

Audrey Van Heest,[‖] Yuzhen Wang,[‖] Liang Zhang, Lucy A. Phillips, Samuel D. Karsen, Christine Nelson, Heather L. Knight, Stuart J. Perper, Stephen O'Brien, Meghan Clements, Victor Z. Sun, Andrew Goodearl, Annette Schwartz Sterman, and Soumya Mitra*

Cite This: *Chem. Biomed. Imaging* 2025, 3, 85−94

Read Online

ACCESS | Metrics & More | Article Recommendations | Supporting Information

ABSTRACT: Disease-recapitulating animal models are valuable tools in preclinical development for the study of compounds. In the case of fibrotic pulmonary diseases such as idiopathic pulmonary fibrosis (IPF), the bleomycin model of lung injury in the mouse is widely used. To evaluate bleomycin-induced changes in the lung, we employed a quantitative, multimodal approach. Using in vivo microcomputed tomography (μCT), we demonstrated radiographic changes associated with disease progression in aeration levels of the lung parenchyma. There exists an unmet need for a quantitative, high-resolution imaging probe to detect pulmonary fibrosis, particularly that can differentiate between inflammatory and fibrotic components of the disease. Matrix remodeling and overexpression of extracellular matrix (ECM) proteins such as collagen and fibronectin are hallmarks of organ fibrosis. A splice variant of fibronectin containing extra domain A (FnEDA) is of particular interest in fibrosis due to its high level of expression in diseased tissue, which is confirmed here using immunohistochemistry (IHC) in mouse and human lungs. An antibody against FnEDA was evaluated for use as an imaging tool, particularly by using in vivo single-photon emission computed tomography (SPECT) and ex vivo near-infrared (NIR) fluorescence imaging. These data were further corroborated with histological tissue staining and fibrosis quantitation based on a Modified Ashcroft (MA) score and a digital image analysis of whole slide lung tissue sections. The fusion of these different approaches represents a robust integrated workflow combining anatomical and molecular imaging technologies to enable the visualization and quantitation of disease activity and treatment response with an inhibitor of the TGFβ signaling pathway.

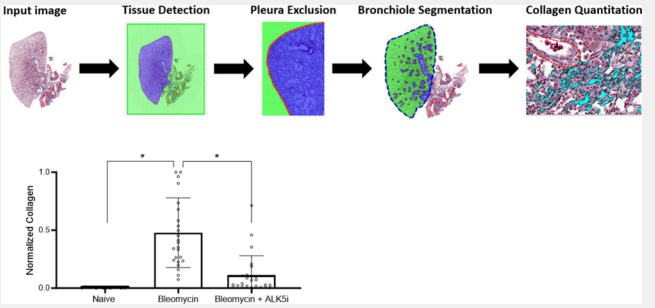

KEYWORDS: *Idiopathic pulmonary fibrosis, fibronectin splice variant, FnEDA, bleomycin, micro-CT, NIR, SPECT, digital whole slide image analysis*

INTRODUCTION

Idiopathic pulmonary fibrosis (IPF) is a chronic and invariably fatal fibrotic lung disorder with an unknown etiology. IPF is one of the most frequently diagnosed interstitial lung diseases (ILDs), and this diagnosis is primarily based on high-resolution computed tomography (HRCT) images from patients exhibiting usual interstitial pneumonia (UIP). Disease pathogenesis remains elusive and controversial, but the prevailing hypothesis assumes an ineffective wound healing response to alveolar epithelial cell injury.[1] The study of human IPF has been aided by the identification of cells, molecular mediators, and processes key to the condition afforded by the development of animal models. Small animal models of lung fibrosis are also essential for the preclinical evaluation of the efficacy of novel antifibrotic compounds. Among these is the bleomycin model—the best-characterized murine model currently in use. The bleomycin mouse model is used for its reproducibility, accessibility, and ease of application. Despite the model's limitation of reproducing the irreversible and progressive nature of IPF, both inflammatory and fibrotic components of the disease induction can be observed, with inflammatory markers elevated prior to fibrotic markers.[2,3]

Current outcome measurements in experimental pulmonary fibrosis animal models involve histopathological and biochemical analyses, such as semiquantitative tissue scores and hydroxyproline content, respectively, but are known to be labor-intensive. While histopathology is a gold-standard for lung fibrosis assessment, digital pathology image analysis-based methods on whole slide images (WSIs) have been developed to mitigate subjectivity in assessing the fibrotic component of

Received: September 4, 2024
Revised: January 6, 2025
Accepted: January 7, 2025
Published: January 17, 2025

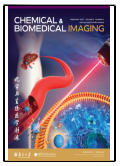

https://doi.org/10.1021/cbmi.4c00065
Chem. Biomed. Imaging 2025, 3, 85−94

the tissue as well as generating quantitative continuous data. Recently, studies have reported on the use of machine learning-based image analysis of WSIs from rodent lung tissue to quantify fibrosis to automate histological scoring tasks.[4,5] In addition to these readouts, in vivo microcomputed tomography (μCT) has been used to quantitate fibrosis severity and treatment response.[6−10] While ex vivo μCT measurements have been validated by comparison to established histologic and physiologic end points,[11] more recent optimizations in in vivo μCT imaging have enabled longitudinal assessments of disease activity and treatment response with each animal acting as their own control.[9,12,13] However, an important challenge with μCT imaging remains. Although μCT scanning is sensitive enough to detect changes in lung tissue density, it cannot distinguish between lung inflammation and fibrosis, as both are manifested by relative increases in tissue density. Discrimination of lung inflammation from fibrosis requires subsequent histological or other sensitive analyses. Imaging collagen, fibronectin, or fibroblast activation protein (FAP) therefore presents an opportunity for characterization of the fibrotic state in the lung. Toward that end, recent studies have reported on the use of molecular imaging probes to monitor Collagen I and FAP in animal models and in ILD patients.[14−20] Fibronectin (FN) is one of the main extracellular matrix (ECM) components, and several studies have demonstrated that alternatively spliced FN isoforms, specifically extra domain A (EDA), is prominently expressed during fibrosis and support myofibroblast activation.[21−24] Further, fibronectin production precedes collagen synthesis in the progression of the disease. We therefore hypothesized that imaging of fibronectin extra domain A (FnEDA) may offer the potential for a readout of specific fibrotic activity. FnEDA is also presented as a potential target for drug delivery, leveraging anti-FnEDA antibody as a payload vehicle, in a mouse model of rheumatoid arthritis and renal fibrosis.[25−27] Here, we describe an antibody-based, FnEDA-targeted imaging probe and demonstrate its ability to detect and quantify pulmonary fibrosis in the mouse bleomycin model as well as monitor therapeutic response with SM16, an ALK5 kinase inhibitor (ALK5i). ALK5i has been published to inhibit myofibroblast activation and cardiac fibrosis in vivo; therefore, it was selected to measure the inhibition of lung fibrosis in the bleomycin injury model.[28,29]

To observe disease progression and assess efficacy of treatments preclinically in animal models of fibrosis, multiple techniques may be required to capture the complexity and multifaceted nature of the disease. To address these challenges, we describe the development of an imaging-based workflow that incorporates a stepwise approach starting with in vivo μCT followed by ex vivo FnEDA near-infrared (NIR) imaging and subsequent downstream histopathology measurements using Modified Ashcroft (MA) scoring by a pathologist[30] and digital image analysis from WSI tissue sections. The ex vivo NIR imaging findings were also validated with single-photon emission computed tomography (SPECT) imaging with a radiolabeled anti-FnEDA IgG. A fully automated deep learning based WSI analysis was used for quantification of collagen changes and evaluation of the antifibrotic effect with treatment. Furthermore, the μCT and NIR imaging protocols do not preclude complementary biochemical measurements of the lung samples and therefore allow a comprehensive multimodal assessment from a single animal.

METHODS

See the Supporting Information for additional information.

Animals, Disease Model, and Treatment

8−10-week-old C57Bl/6 male mice (8−10 weeks old) from Jackson Laboratory (Bar Harbor, ME) were used in the study. All animal studies were performed under protocols approved by the AbbVie Bioresearch Center Institutional Animal Care and Use Committee (IACUC) in accordance with the Principles of Laboratory Animal Care.

On day 0, mice in the diseased groups were dosed with 2 U/kg of bleomycin sulfate via oropharyngeal administration (Meitheal Pharmaceuticals, cat. no. 71288-106-10, Chicago, IL). Naïve animals were dosed with PBS via oropharyngeal administration (Gibco Thermofisher Scientific, Waltham, MA). Enrollment of animals was determined based on day 7 % body weight loss of 5−20% from day 0. Animals were monitored for body weight on days 3, 7, 10, 14, 18, and 21.

The treatment group was dosed orally with 45 mg/kg of the ALK5i,[28,29,31,32] formulated in Captisol, once daily beginning on day 8. Similarly, the untreated bleomycin group was dosed with Captisol without ALK5i.

In vivo μCT images of the lungs were acquired on day 20 of disease progression using the MILabs U-CT (Utrecht, Netherlands). The mice were anesthetized using isoflurane and subsequently laid in a prone position on the imaging bed. The following settings were used: X-ray voltage 50 kV, current 0.21 mA, steps 0.750°, frame averaging of 1, 16 projections/step, and 20 ms exposure time, resulting in an estimated radiation dose of 2662 mGy. Following image acquisition, the images were reconstructed using the Hann filtered back-projection algorithm (MILabs Reconstruction software; MILabs). A voxel width of 40 μm was used, and respiratory gating was applied during reconstruction. Analysis of the μCT images was completed by using VivoQuant software (Invicro, Boston, MA). A 0.2 mm anisotropic Gaussian filter was applied to the image. The 3D ROI tool was then used to create a region of interest (ROI) including the lungs. A neighborhood threshold was applied to this ROI within the range of −860 to 0 Hounsfield Units (HU), and a density histogram of this ROI was exported for further analysis.

Animals were dosed with anti-FnEDA-800CW IgG on day 18 intravenously at 6 mg/kg. To evaluate in vivo targeting specificity, a cohort of animals was also coadministered anti-FnEDA-800CW (6 mg/kg) with competing unlabeled anti-FnEDA (60 mg/kg). 72 h after dosing, mice were euthanized, and the lungs were resected for NIR imaging. The anti-FnEDA monoclonal IgG antibody (mAb) used in this manuscript was generated at AbbVie, and its characterization has been described previously.[26,27] Anti-FnEDA mAb specifically binds to fibronectin containing the splice insertion of EDA with no binding to plasma fibronectin that does not contain the FnEDA. Near-infrared (NIR) imaging was performed on a Pearl Imager (Li-Cor, Lincoln, NE) and analyzed according to the mean fluorescence intensity of each image using Image Studio (Li-Cor, Lincoln, NE) as described previously.[33]

In parallel, additional animals were dosed with ^{111}In-anti-FnEDA IgG on day 18 intravenously. 72 h after dosing, in vivo SPECT-CT images were acquired using a U-SPECT/CT system (MILabs, Netherlands). Images were analyzed by using PMOD software (PMOD Technologies, Zurich, Switzerland). Following imaging, the animals were euthanized, and organs were collected for radioactivity measurement using a gamma well counter (PerkinElmer, Waltham, Massachusetts).

Left lung lobes from diseased or naïve mice were harvested and routinely processed for FnEDA expression assay via immunohistochemistry (IHC) protocols described in the Supporting Information. Similar IHC methods were adopted to evaluate FnEDA expression in human lung, both IPF and NAT (normal adjacent tissue) from a patient with Non-Small Cell Squamous Cell Carcinoma.

Anti-human IHC and NIR fluorescence microscopy to detect local lung distribution of the dosed anti-FnEDA-800CW IgG was

https://doi.org/10.1021/cbmi.4c00065
Chem. Biomed. Imaging 2025, 3, 85−94

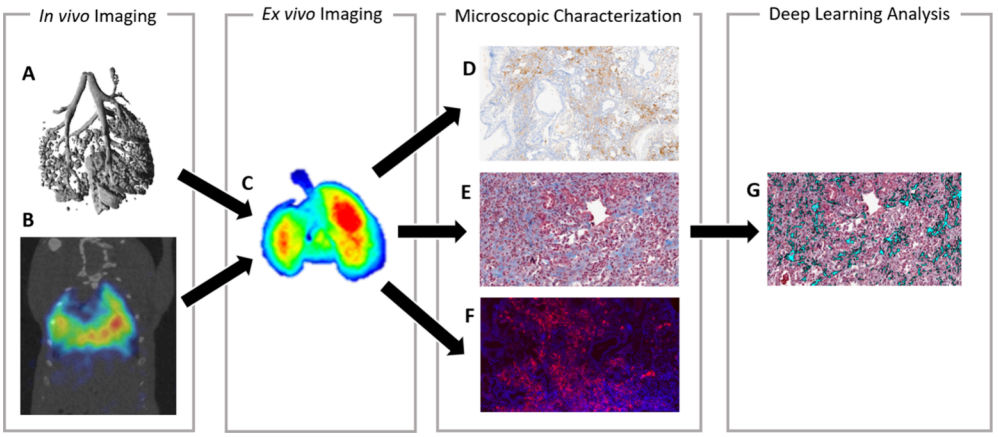

Figure 1. Multifaceted workflow for characterization of bleomycin-induced pulmonary fibrosis. (A) In vivo μCT imaging quantifies lung density and tissue aeration. (B) SPECT imaging allows for visualization of anti-FnEDA IgG uptake using radioactive labeling. (C) Ex vivo NIR imaging reflects the FnEDA levels via fluorescence. (D) Chromogenic IHC detects anti-FnEDA IgG, visualized through the brown DAB chromagen. (E) Masson's Trichrome stains collagen blue, allowing for histopathology scoring of fibrosis via Modified Ashcroft score. (F) NIR microscopy of tissue slides allows microscopic visualization of FnEDA localization. (G) Image analysis detects blue-stained collagen to quantify collagen deposition.

performed, and slides were digitally imaged using the Pannoramic 250 whole slide scanner (3DHistech, Budapest, Hungary).

Serial sections were stained with hematoxylin and eosin (H&E) and Masson's Trichrome using Leica Biosystems Autostainer (Wetzlar, Germany). H&E slides were qualitatively evaluated and semiquantitatively scored by a pathologist for inflammation using a 0−5 scale (0 = none, 1 = minimal, 2 = mild, 3 = moderate, 4 = marked, and 5 = severe). Masson's Trichrome slides were scored using the Modified Ashcroft (MA) 0−8 scale,[25] and whole slide images were subsequently used for quantitative digital image analysis to identify the blue-stained regions of newly formed collagen via application of a four-step sequence of algorithms designed and trained in Visiopharm (Visiopharm A/S, Horsholm, Denmark; manuscript in preparation).

Statistical Analysis

For lung inflammation and Modified Ashcroft semiquantitative scores, groups were tested for significance ($p < 0.05$) using nonparametric Kruskall Wallis ANOVA and Dunn's multiple comparison tests. For other readouts, groups were tested for significance ($p < 0.05$) using Brown-Forsythe and Welch ANOVA tests with Dunnett's post-test to correct for multiple comparisons, using GraphPad Prism software (San Diego, CA).

RESULTS

Primary data collected in this study came from in vivo μCT, SPECT, NIR imaging, and histopathology scoring and were aggregated from 4 individual studies. This process is illustrated in Figure 1, where in vivo μCT and SPECT was succeeded by ex vivo NIR fluorescence imaging, both of which provide macroscopic views of the tissue. Following these procedures, serial sections of the left lung lobe were used to generate three forms of histopathological images: H&E, Masson's Trichrome, and antihuman IHC for detection of FnEDA mAb. Whole slide images of sectioned tissue with Masson's Trichrome staining were also analyzed through digital image analysis. Supplementary data were also collected, reflecting the animal body weight, lung weight, and lung hydroxyproline content (Figure S1).

In vivo μCT images were used to assess the density and aeration levels of the lung tissue at day 20. Figure 2A compares 3D rendered images of a naïve and bleomycin animal, where the tissue shown is of a density that reflects adequate access to air (normo-aerated). The image from the bleomycin animal clearly shows that fewer tissues are sufficiently aerated. This is quantitatively reflected through Figure 2B, where the volume of tissue that is normo-aerated is calculated for each animal, with at least 15 animals in each group. In the bleomycin group,

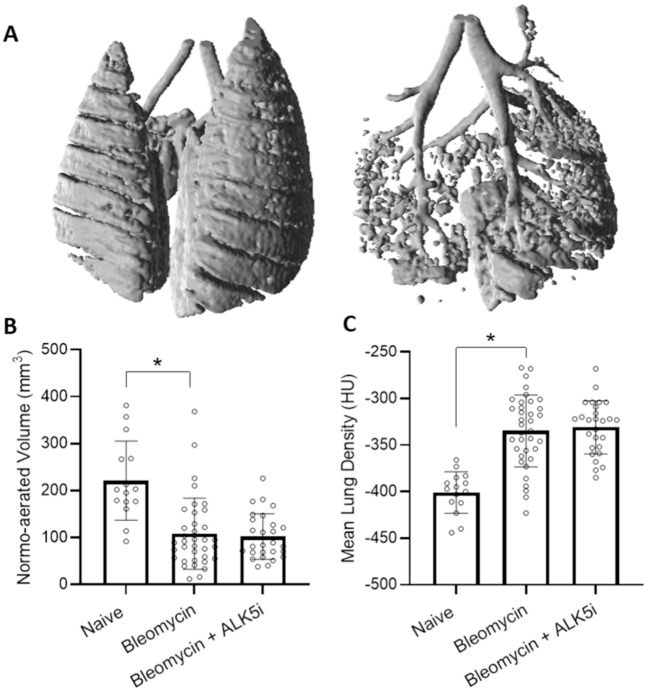

Figure 2. In vivo micro-CT imaging. (A) 3D renderings of μCT images allow visualization of aerated tissue, with a naïve animal shown on the left and a bleomycin animal shown on the right. The bleomycin animal rendering indicates a reduction in aerated tissue as compared to the naïve. (B) Calculation of the volume of tissue which falls within the density range designated as aerated (−860 to −435 HU) is plotted here, demonstrating reduced aerated lung volume with disease ($p < 0.05$) and no improvement with treatment. N = at least 15, including data from separate studies. (C) Mean lung density of the tissue in the range of −860 to 0 HU is plotted here, indicating greater density seen in the bleomycin group as compared to the naïve group ($p < 0.05$) with no improvement associated with treatment. N = at least 15, including data from separate studies. *$p < 0.05$. Data are presented as mean (±SD).

https://doi.org/10.1021/cbmi.4c00065
Chem. Biomed. Imaging 2025, 3, 85−94

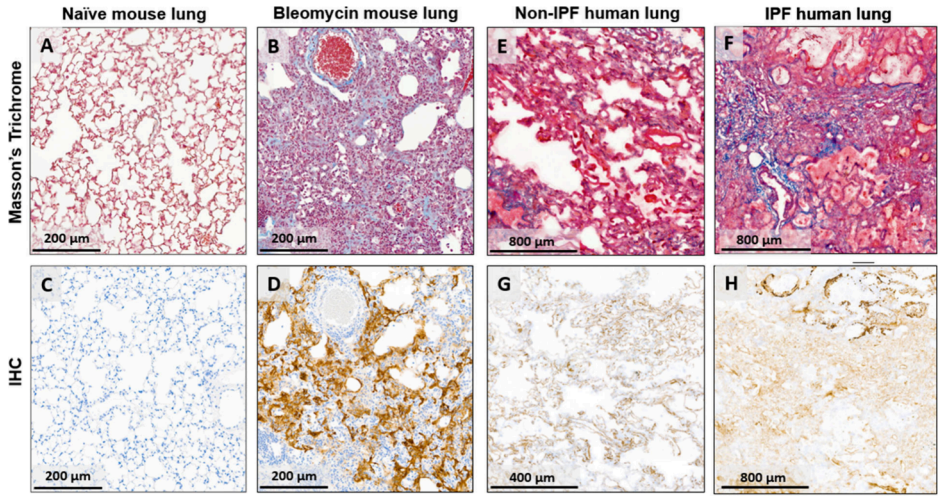

Figure 3. Histological assessment of collagen and FnEDA expression. (A, B) Fibrotic regions can be observed through blue-stained collagen with Masson's Trichrome, which allows for visualization of the effects of bleomycin. Increased deposition of collagen in the lung parenchyma is shown in the untreated, bleomycin group as compared to naïve. (C, D) Consecutive images immunolabeled with FnEDA show increased expression of FnEDA in the untreated group as compared to naïve. (E, F) Confirming the translational relevance of the bleomycin murine model, human IPF lung also shows increased collagen deposition on Trichrome stained sections and markedly greater FnEDA expression (G, H) as compared to normal adjacent lung tissue from a patient without IPF (Nonsmall Squamous Cell Lung Carcinoma). These are representative images from approximately the same regions of the tissue to demonstrate the close alignment of anti-FnEDA and trichrome staining; they do not illustrate close alignment due to inherent variability in tissue morphology when slides are sectioned from a block at different times.

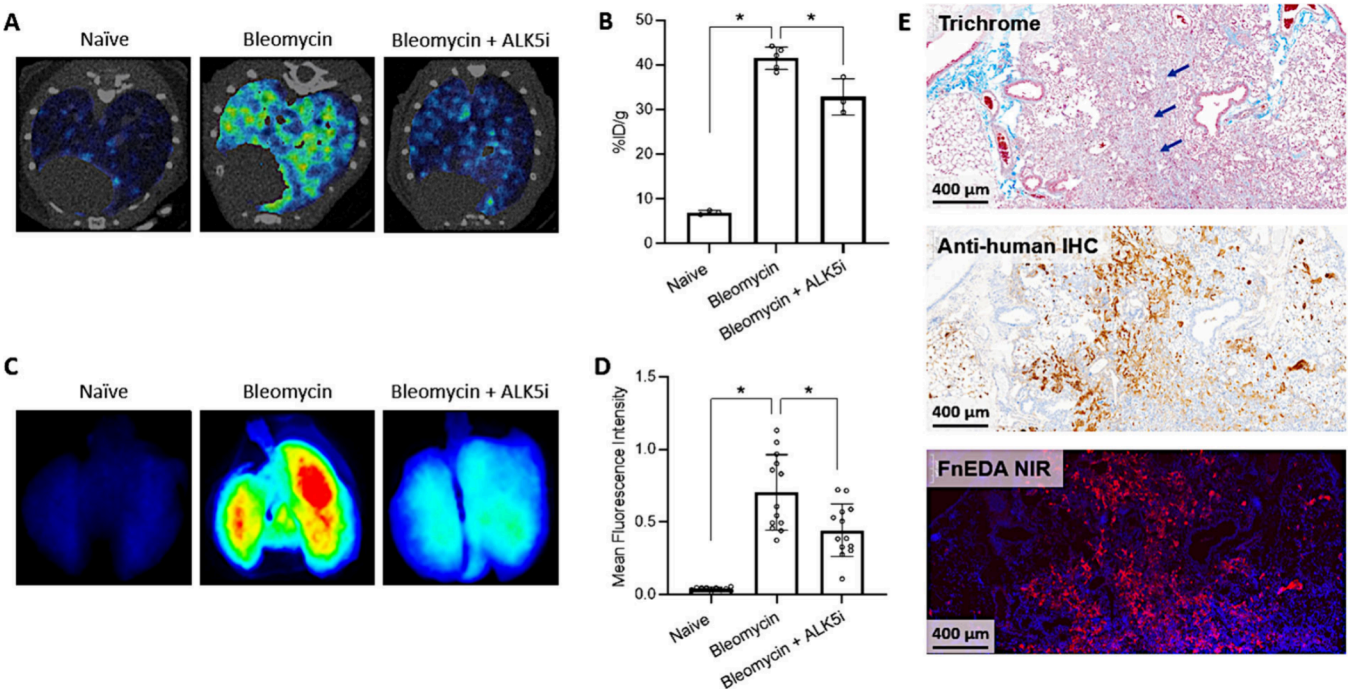

Figure 4. Validation of anti-FnEDA IgG as an imaging marker of fibrosis disease activity in mouse lung. (A) In vivo SPECT images are shown here using μCT-derived lung segmentation to illustrate radioactive signal within the lung. Low signal is seen in the naïve group as compared to the bleomycin and ALK5i groups, indicating less FnEDA detected. $N = 3$. (B) Measurements of radioactive signal from the gamma well counter are expressed here as percent injected dose per gram of tissue (%ID/g). Signal is shown to increase with disease, and the ALK5i treatment group is shown to reduce signal compared to the untreated group. $N = 5$. (C) Ex vivo NIR images show low signal in the naïve group, high signal in the bleomycin group, and reduced signal in the ALK5i treatment group. $N = 5$. (D) Mean fluorescence intensity from the NIR images is shown here, agreeing with the trends observed visually. N = at least 10, including data from 2 separate studies. (E) Subsequent tissue sections from an untreated bleomycin lung are shown, with Masson's Trichrome staining, antihuman IHC, or NIR fluorescence. Disease-associated extracellular matrix proteins, either collagen or fibronectin, can be seen in the same regions in each of the 3 images. Collagen is stained blue (indicated by arrow) by trichrome staining. FnEDA is indicated by the brown color in the IHC image and bright pink signal in the NIR image. *$p < 0.05$. Data are presented as mean (±SD).

there is a decrease in normo-aerated volume as compared to the naïve group (naïve 221 ± 84 mm^3 vs bleomycin 108 ± 76 mm^3, $p < 0.05$). Further, there is positive shift in mean lung density associated with disease, indicating that tissue becomes

https://doi.org/10.1021/cbmi.4c00065
Chem. Biomed. Imaging 2025, 3, 85−94

more dense (naïve −401 ± 22 HU vs bleomycin −335 ± 39 HU, $p < 0.05$) (Figure 2C). However, compared to the bleomycin group, there are no signs of change in tissue aeration associated with ALK5i treatment (102 ± 49 mm^3), as well as no effect in lung density associated with treatment (−331 ± 28 HU).

Traditional readouts, such as lung and body weight and hydroxyproline levels, were also measured (Figure S1). Left lung lobes weight measurements at day 21 indicate an increase in weight with disease and no treatment effect (naïve 60 ± 7 mg vs bleomycin 123 ± 22 mg, $p < 0.05$, N = at least 5). Body weight measurements, as expressed by percent change from day 0 to 21 of disease, also show decreased body weight in the bleomycin and bleomycin + ALK5i groups as compared to the naïve group (naïve vs bleomycin $p < 0.05$, N = at least 10) but no improvement with ALK5i treatment. However, hydroxyproline content, which is a marker of collagen deposition, is observed to decrease in diseased mice with ALK5i treatment as compared to untreated bleomycin mice (bleomycin 11 ± 2.9 vs bleomycin + ALK5i 7.4 ± 1.8, $p < 0.05$, N = at least 10).

The lack of lung tissue aeration changes with ALK5i treatment, as reported by in vivo μCT, motivated the evaluation of a molecular marker that would be more sensitive to the changes in matrix content. Toward that end, IHC was performed in mouse and human lung samples to assess FnEDA expression in fibrotic regions of diseased lung samples and assess the value of monitoring FnEDA changes as a readout of fibrotic activity in rodent models and human tissue. Histologic evaluation of trichrome-stained mouse lung tissue revealed significant collagen deposition at day 21 postbleomycin induction vs healthy naïve control (Figure 3A,B), and we observed pronounced FnEDA expression in the fibrotic regions performed on a sequential tissue section (Figure 3D). Conversely, lung samples in naive mice demonstrated a conspicuous lack of FnEDA (Figure 3C). Relevance of FnEDA to human IPF is demonstrated here, where a lung sample from a human IPF patient shows increased collagen and FnEDA expression as compared to normal adjacent non-IPF lung from a patient with nonsmall-cell squamous-cell lung carcinoma (Figure 3E−H). The FnEDA expression is observed to be closely associated with regions of active fibrosis, known as fibroblastic foci.

To characterize FnEDA expression in the early inflammatory phase of the bleomycin model, an FnEDA IHC time course was quantitatively evaluated from day 1 through day 7, and lung inflammation was semiquantitatively scored by a pathologist (Figure S2). Inflammatory infiltrates are observed as early as day 1 post-bleomycin administration and thereafter show a progressive and statistically significant increase from day 3 through day 7 compared to naive mice. Inflammatory infiltrates are composed of macrophages and lymphocytes admixed with occasional neutrophils. FnEDA expression shows a similar progressive, albeit slightly delayed, increase with statistical significance achieved by day 5 through day 7 relative to naïve mice. FnEDA expression was first observed in the early time points (days 1−3) as linear extracellular deposits in the morphologically normal alveolar interstitium adjacent to the bleomycin-damaged areas of lung. By days 5−7, extracellular FnEDA expression was also observed within the damaged regions of the lung, intimately associated with areas of inflammation. By day 21, robust extracellular FnEDA expression aligned with regions of collagen deposition on trichrome stained sections, while treatment with ALK5 inhibitor ameliorated the FnEDA expression (Figure S3).

FnEDA expression in the bleomycin model can be visualized on a macroscopic level both in vivo by using SPECT imaging and ex vivo by using NIR imaging. SPECT imaging revealed signal from the lung, as defined using CT segmentation, shown in Figure 4A, where low radioactive signal is seen in the naïve group and high signal is seen in the untreated bleomycin group. The ALK5i treatment is shown to result in some reduction in the radioactive signal. Ex vivo gamma counts were used to calculate the mean percent injected dose per gram (% ID/g) for each lung, quantifying the radioactive signal and indicating the relative expression of FnEDA (Figure 4B). These values validate what was observed in the SPECT images, where %ID/g increased in the diseased groups (naïve 3 ± 7% vs bleomycin 42 ± 2.5%, $p < 0.05$, $N = 5$). Further, the ALK5i treatment moderately lowered the % ID/g to 33 ± 4.1 ($p < 0.05$). Uptake of ^{111}In-anti-FnEDA IgG for all organs measured are included in Figure S4A,B and demonstrate specificity of the radioactive signal using blocking with the addition of unlabeled anti-FnEDA IgG. Collectively, this data shows that the distribution of ^{111}In-anti-FnEDA Ig was preferentially localized to the fibrotic lungs of the mice and that FnEDA assessment is a sensitive molecular readout of disease severity. While SPECT imaging offers the potential for longitudinal imaging in vivo, ex vivo NIR imaging can be beneficial for its lack of ionizing radiation, higher resolution, and ease of downstream tissue handling without radioactivity safety protocols. NIR fluorescence images afford a quick visual representation of fibrosis, specifically fibronectin content, with fluorescence indicating the presence of FnEDA IgG labeled with the IRdye800CW (Figure 4C). Low fluorescent signal is seen in the naïve group, which is contrasted by high signal in the untreated bleomycin group and a moderate but significant reduction in intensity associated with treatment. Information provided by the NIR images reflects quantitation of FnEDA present in the lung tissue and can be distilled to a single value representing the whole lung: the mean fluorescence intensity (MFI) (Figure 4D). The signal was normalized to a scale from 0 to 1, and we observe that the MFI increased from 0.04 ± 0.01 in the naïve group to 0.70 ± 0.26 with disease ($p < 0.05$). NIR imaging of lungs excised from mice treated with ALK5i indicates a reduction in anti-FnEDA IgG uptake associated with treatment (bleomycin 0.70 ± 0.26 vs bleomycin + ALK5i 0.44 ± 0.18, $p < 0.05$, N = at least 10). The increase in the FnEDA NIR signal with bleomycin induction and the decrease in signal with treatment are consistent with the changes in FnEDA expression observed by IHC in mouse lungs illustrated in Figure S3. We sought to confirm that these NIR signals were due to the in vivo targeting of 800CW-labeled anti-FnEDA IgG, and toward that end, we performed NIR microscopy and antihuman IHC detection of the anti-FnEDA IgG in histologic lung sections. H&E, Masson's Trichrome, antihuman IHC, and NIR microscopy were performed in sequential histology sections (Figure 4E). As visualized in the image panel, the light blue stained region in the Trichrome image reflects new collagen deposition in fibrotic regions which align with areas of the anti-FnEDA IgG distribution as reported by the NIR fluorescence and antihuman IHC. To further confirm the specificity of the NIR signal, we added 2 groups for ex vivo whole lung NIR imaging which had been dosed with excess unlabeled anti-FnEDA IgG in addition to the 800CW labeled reagent. When the 800CW-anti-FnEDA IgG + anti-FnEDA

https://doi.org/10.1021/cbmi.4c00065
Chem. Biomed. Imaging 2025, 3, 85−94

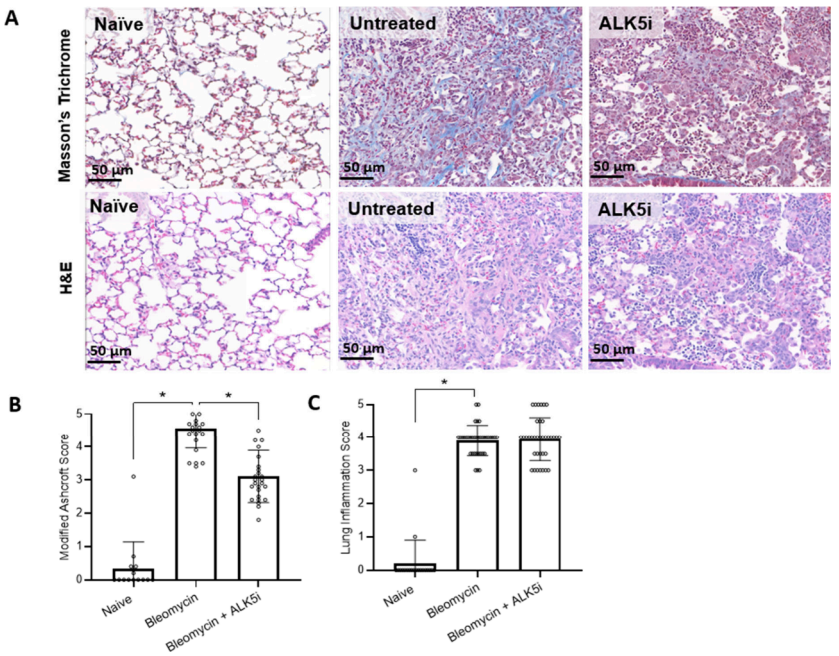

Figure 5. Histopathology scoring of disease activity using Masson's Trichrome and H&E staining. (A) Images of Masson's Trichrome-stained and H&E-stained tissue sections, shown here at 200× magnification. Masson's Trichrome staining demonstrates decreased collagen deposition with treatment as shown in blue. The inflammatory component of the disease can be visualized in both Masson's Trichrome-stained and H&E-stained tissue sections. (B) Histopathology scoring of Masson's trichrome images indicates treatment-associated improvement in the modified Ashcroft score as compared to the untreated bleomycin group ($p < 0.0001$). N = at least 15, including data from 3 separate studies. (C) Histopathology scoring of inflammation on H&E images indicated that the ALK5i treatment has no effect on lung inflammation. N = at least 20, including data from 4 separate studies. *$p < 0.05$. Data are presented as mean (±SD).

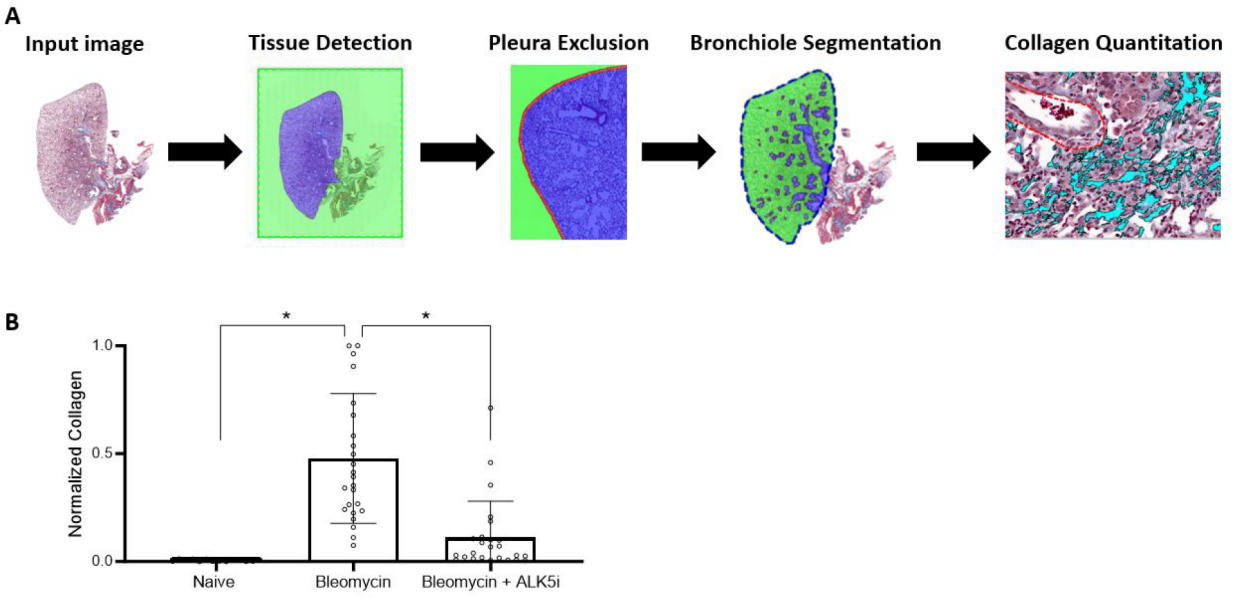

Figure 6. Whole slide image analysis. (A) The image analysis process is shown here, starting from a Masson's Trichrome-stained whole slide image. Identification and labeling of the lung tissue and background is first performed. Next, the pleura and associated fibrosis at the edge of the tissue is delineated and excluded from the ROI. The bronchioles are then segmented, along with pre-existing collagen surrounding this structure, which is stained dark blue. The bronchioles and pre-existing collagen are also excluded from the lung tissue ROI. Finally, newly developed collagen, as indicated by light-blue staining, is segmented and quantified as a fraction of the total lung tissue area. (B) Collagen content is normalized on a scale from 0 to 1 using the maximum collagen fraction in each study and reported as normalized collagen, which is reflective of bleomycin-induced disease. N = at least 20, including data from 3 separate studies. *$p < 0.05$. Data are presented as mean (±SD).

IgG is subtracted from the signal with only labeled IgG, the resultant signal can be considered specific to the targeting epitope (Figure S4C,D,E). A correlation of FnEDA NIR MFI to lung density and norm-aerated volume measurements from micro-CT exhibited 0.48 and −0.55 (Pearson r), respectively (Figure S5A,B).

Masson's Trichrome affords the benefit of illustrating both the fibrotic component and the density of the bleomycin-

https://doi.org/10.1021/cbmi.4c00065
Chem. Biomed. Imaging 2025, 3, 85−94

damaged lungs and is a traditional histochemical stain for scoring collagen deposition in tissues. Images of lung sections from bleomycin animals show increased light blue staining of newly synthesized collagen and higher cell density in the lung parenchyma, as compared to naïve animals (Figure 5A). Images from the ALK5i treatment group show reduced collagen staining but no change in cell density as compared to the untreated bleomycin group. Pathologist scoring using the modified Ashcroft score on a scale from 0 to 8 indicates that the bleomycin model results in significant lung fibrosis compared to the naïve group (bleomycin 4.6 ± 0.60 vs naïve 0.34 ± 0.79, $p < 0.05$, N = at least 15) (Figure 5B). Scoring also confirms a treatment-associated reduction in lung fibrosis (bleomycin 4.6 ± 0.60 vs bleomycin + ALK5i 3.1 ± 0.79, $p < 0.05$). A correlation of the MA score to NIR MFI was calculated to be 0.76 (Spearman r), suggesting a significant positive relationship between the pathologist score and the FnEDA lung uptake (Figure S5C). H&E-stained sections were used to evaluate inflammation in the lung tissue. Images show infiltration of inflammatory cells, consisting predominantly of macrophages mixed with fewer lymphocytes and occasional neutrophils, resulting in higher cell density in diseased lungs. Pathologist scoring for inflammation on a scale from 0 to 5 indicates significantly higher inflammation in the untreated bleomycin group as compared to naïve (bleomycin 3.9 ± 0.4 vs naïve 0.20 ± 0.70, $p < 0.05$, N = at least 20) (Figure 5C). Further, unlike fibrosis scores, inflammation was not reduced by treatment (bleomycin, 3.9 ± 0.46 vs bleomycin + ALK5i, 3.9 ± 0.65, $p = 0.99$).

The newly formed collagen visible in Masson's Trichrome images can be quantified using digital image analysis. Using a whole slide image, the sequence of algorithms identifies the tissue, excludes the pre-existing collagen around airways and vessels and in the pleura, and then captures the light blue newly formed collagen (Figure 6A). The output of this algorithm provides a measure of newly formed collagen as a percentage of the whole tissue area. Reporting these values, the bleomycin group is found to have greater collagen content than both the naïve and bleomycin + ALK5i groups (bleomycin 0.48 ± 0.30 vs naive 0.058 ± 0.048 vs bleomycin + ALK5i 0.11 ± 0.17, $p < 0.05$, N = at least 20) (Figure 6B). These findings agree well with the pathologist-reported values for fibrosis through the modified Ashcroft score, as well as the mean fluorescence intensity of NIR images, which also reflects the severity of fibrosis.

■ DISCUSSION

IPF is characterized by extensive lung tissue scarring, variable immune cell infiltration, and extracellular matrix remodeling. Although the bleomycin model does not completely recapitulate human IPF, it remains the most common and important animal model to study this disease. Oropharyngeal administration of bleomycin in mice results in the time-dependent development of fibrosis. The early phase post bleomycin administration is characterized by acute lung injury and inflammation, which is observed to last between day 1 and day 7.[34,35] This inflammatory phase is followed by active fibrosis, between days 7 to 14, and late fibrosis, between days 21 to 28.[34−36] To analyze the dynamic and complex nature of disease pathophysiology in this model, we report a comprehensive assessment of macroscopic-scale functional changes with μCT and an ECM imaging marker, respectively, followed by a histopathological evaluation based on traditional scoring and digital image analysis that enables rapid quantitation of lung fibrosis.

Besides fibrosis, several studies have reported on the use of μCT to evaluate disease progression and therapy effects in other models of lung diseases, including cancer and emphysema.[7,37] Further, lung μCT delivers visual and quantitative three-dimensional information about the whole lung, including regional differences with high resolution and sensitivity, yielding translational data that align well with imaging assessments routinely performed in lung disease patients. Analysis of the aerated lung volume as reported in our study is a parameter that probably best corresponds to the total lung capacity measured by pulmonary functional tests. While in vivo μCT images show significance in decreased normo-aerated volume and increased mean lung density with disease induction, there is no change in these readouts in response to treatment (Figure 2). Inflammation and fibrosis both manifest as relative increases in tissue density, which can be detected by μCT scanning, and although μCT scans are sensitive enough to detect changes in lung tissue density, the current techniques do not distinguish between lung inflammation and fibrosis. As shown in the pathology scores (Figure 5C), although the severity of fibrosis was found to be diminished by ALK5i treatment, the inflammatory component of the disease was found to be unchanged. Therefore, μCT may not be sensitive to the improvement of fibrosis because it is overshadowed by the inflammatory component, which maintains the higher tissue density. Discrimination of lung inflammation from fibrosis therefore needs subsequent histological and other sensitive analyses, such as an imaging marker that offers a quantitative readout of extracellular matrix changes.

As a protein integral to fibrosis with evidence of expression prior to collagen deposition in the disease course, fibronectin isoforms present a unique opportunity for probing tissue to assess fibrosis.[22,23] A recent study demonstrated targeting with the identical anti-FnEDA IgG in a mouse model of collagen-induced arthritis,[27] while a dual variable domain Ig (DVD-Ig) construct with one moiety targeting FnEDA and a second moiety to TGF-β was shown to demonstrate focal uptake in a fibrotic kidney mouse model and also reduced renal fibrosis with the targeted delivery of the neutralizing TGF-β.[26] Here, monoclonal IgG binding to FnEDA is detected by three methods: through NIR imaging of fluorescent 800CW conjugated to IgG, SPECT imaging of radioactive ^{111}In conjugated to IgG, and chromogenic antihuman IHC. Comparison of microscopic NIR images with antihuman IHC offers additional confirmation of IgG-800CW as an imaging probe. Further, comparison with Masson's Trichrome collagen staining allows for validation of FnEDA as a target for detection of fibrotic regions. While tissue sections selected for Masson's Trichrome staining represent the fibrosis region in the tissue, whole tissue NIR imaging provides quantitative readouts of the entire organ, rather than select regions. Similarly, μCT, though not sensitive to changes in fibrosis without a concomitant reduction in the inflammatory burden, provides a quantitative readout of tissue aeration of the whole lung. The differences and complementary value in these different readouts is captured in Figure S5, where we report a significant correlation of 0.76 between MA and NIR quantitation in contrast to a lower r value between the NIR and μCT readouts. Importantly, both μCT and NIR imaging do not preclude further downstream analyses with excised lung

https://doi.org/10.1021/cbmi.4c00065
Chem. Biomed. Imaging 2025, 3, 85−94

tissue samples. In contrast, hydroxyproline, a traditional but variable measure of assessing collagen content, is quantitative but requires digestion of the lung lobe, restricting the analysis of the whole organ.

Pathologists can provide nuanced perspectives on tissue; however, generating MA scores covering an entire cross section of the lung can be time prohibitive. To address this challenge, an image analysis sequence of algorithms of whole slide images was developed to automate the quantitation of collagen in the lungs. Utilizing a deep learning algorithm to segment the lung tissue sections and limiting the image analysis to regions of active fibrosis, we observed a significant correlation of newly formed collagen content with MA scores. This approach lays the foundation for a rapid and reliable quantitative assessment of disease activity in histological sections.

With a disease as complex and dynamic as IPF, it would be valuable to evaluate changes in the same animal over time, especially in response to treatment. Therefore, integrating FnEDA imaging through SPECT allows for quantitative evaluation of the fibrotic component in vivo by labeling with a radioactive tracer. This modality affords a longitudinal, macroscopic assessment of the disease, including the ability to assess fibrotic changes in response to treatment.

CONCLUSIONS

In summary, we present a comprehensive process that effectively characterizes the fibrotic and inflammatory components of a bleomycin-induced fibrosis mouse model in response to an ALK5i treatment. ALK5i treatment is shown to result in a nuanced improvement. Treatment-associated reduction in fibrosis is indicated by reduced fibronectin and collagen deposition as shown through SPECT and NIR imaging of FnEDA, histopathology scoring and digital image analysis of Masson's Trichrome-stained tissue section images, and antihuman chromogenic IHC tissue sections. We demonstrate that traditional histopathology scoring can be used in conjunction with more recently developed imaging techniques that seek to quantify the disease state while reducing the labor, time, and training needed, allowing for resources to be spent on more robust investigations. These results and the workflow provide a reference point for future investigations in preclinical models of pulmonary fibrosis.

ASSOCIATED CONTENT

Supporting Information

The Supporting Information is available free of charge at https://pubs.acs.org/doi/10.1021/cbmi.4c00065.

Additional experimental details: fluorescence and radio labeling of Anti-FnEDA IgG, animal disease model and treatment, in vivo SPECT/CT imaging, IHC, imaging analysis, and hydroxyproline assay; Figure S1: traditional end point animal and lung tissue characterization; Figure S2: lung inflammation and FnEDA expression in the early inflammatory phase of the bleomycin model; Figure S3: IHC expression of FnEDA; Figure S4: tissue uptake of anti-FnEDA IgG; Figure S5: Correlation of normo-aerated volume, mean lung density, and modified Ashcroft Score to NIR imaging-based MFI with anti-FnEDA-800CW (PDF)

AUTHOR INFORMATION

Corresponding Author

Soumya Mitra − *AbbVie Bioresearch Center, Worcester, Massachusetts 01605, United States;* orcid.org/0009-0006-1293-9340; Email: soumya.mitra@abbvie.com

Authors

Audrey Van Heest − *AbbVie Bioresearch Center, Worcester, Massachusetts 01605, United States*

Yuzhen Wang − *AbbVie Bioresearch Center, Worcester, Massachusetts 01605, United States*

Liang Zhang − *AbbVie Bioresearch Center, Worcester, Massachusetts 01605, United States*

Lucy A. Phillips − *AbbVie Bioresearch Center, Worcester, Massachusetts 01605, United States*

Samuel D. Karsen − *AbbVie Bioresearch Center, Worcester, Massachusetts 01605, United States*

Christine Nelson − *AbbVie Bioresearch Center, Worcester, Massachusetts 01605, United States*

Heather L. Knight − *AbbVie Bioresearch Center, Worcester, Massachusetts 01605, United States*

Stuart J. Perper − *AbbVie Bioresearch Center, Worcester, Massachusetts 01605, United States*

Stephen O'Brien − *AbbVie Bioresearch Center, Worcester, Massachusetts 01605, United States*

Meghan Clements − *AbbVie Bioresearch Center, Worcester, Massachusetts 01605, United States*

Victor Z. Sun − *AbbVie Bioresearch Center, Worcester, Massachusetts 01605, United States*

Andrew Goodearl − *AbbVie Bioresearch Center, Worcester, Massachusetts 01605, United States*

Annette Schwartz Sterman − *AbbVie Bioresearch Center, Worcester, Massachusetts 01605, United States*

Complete contact information is available at: https://pubs.acs.org/10.1021/cbmi.4c00065

Author Contributions

‖A.V.H. and Y.W. contributed equally to this work. A.V.H., Y.W., L.Z., M.C., V.Z.S., A.S.S., A.G., and S.M. designed the research. A.V.H., C.N., L.Z., S.J.P., S.O.B., H.L.K., and Y.W. performed the experiments. A.V.H., Y.W., L.Z., L.A.P., S.D.K., and S.M. analyzed the data. A.V.H., Y.W., L.A.P., and S.M. prepared the figures and wrote the manuscript. All authors reviewed the manuscript.

Notes

The authors declare the following competing financial interest(s): Y.W., L.A.P., S.D.K., C.N., H.L.K., S.J.P., M.C., S.O.B., A.G., A.S.S., A.G., and S.M. are employees of AbbVie. A.V.H., V.Z.S., and L.Z. were employees of AbbVie at the time of the study.

ACKNOWLEDGMENTS

We acknowledge Abby McCarthy and Alhussein Farouk for their help in immunohistochemistry of the mouse lung tissue sections. The design, study, and financial support for the experiments were provided by AbbVie. AbbVie participated in the interpretation of data, review, and approval of the publication.

REFERENCES

(1) Ahluwalia, N.; Shea, B. S.; Tager, A. M. New Therapeutic Targets in Idiopathic Pulmonary Fibrosis. Aiming to Rein in Runaway Wound-Healing Responses. *Am. J. Respir Crit Care Med.* **2014**, *190* (8), 867−78.

(2) Moeller, A.; Ask, K.; Warburton, D.; Gauldie, J.; Kolb, M. The bleomycin animal model: a useful tool to investigate treatment options for idiopathic pulmonary fibrosis? *Int. J. Biochem. Cell Biol.* **2008**, *40* (3), 362−82.

(3) Jenkins, R. G.; Moore, B. B.; Chambers, R. C.; Eickelberg, O.; Königshoff, M.; Kolb, M.; et al. An Official American Thoracic Society Workshop Report: Use of Animal Models for the Preclinical Assessment of Potential Therapies for Pulmonary Fibrosis. *Am. J. Respir. Cell Mol. Biol.* **2017**, *56* (5), 667−79.

(4) Seger, S.; Stritt, M.; Vezzali, E.; Nayler, O.; Hess, P.; Groenen, P. M. A.; et al. A fully automated image analysis method to quantify lung fibrosis in the bleomycin-induced rat model. *PLoS One.* **2018**, *13* (3), No. e0193057.

(5) Heinemann, F.; Birk, G.; Schoenberger, T.; Stierstorfer, B. Deep neural network based histological scoring of lung fibrosis and inflammation in the mouse model system. *PLoS ONE* **2018**, *13*, e0202708.

(6) Cavanaugh, D.; Travis, E. L.; Price, R. E.; Gladish, G.; White, R. A.; Wang, M.; et al. Quantification of bleomycin-induced murine lung damage in vivo with micro-computed tomography. *Acad. Radiol.* **2006**, *13* (12), 1505−12.

(7) De Langhe, E.; Vande Velde, G.; Hostens, J.; Himmelreich, U.; Nemery, B.; Luyten, F. P.; et al. Quantification of lung fibrosis and emphysema in mice using automated micro-computed tomography. *PLoS One.* **2012**, *7* (8), No. e43123.

(8) Zhou, Y.; Chen, H.; Ambalavanan, N.; Liu, G.; Antony, V. B.; Ding, Q.; et al. Noninvasive Imaging of Experimental Lung Fibrosis. *Am. J. Respir. Cell Mol. Biol.* **2015**, *53* (1), 8−13.

(9) Vande Velde, G.; Poelmans, J.; De Langhe, E.; Hillen, A.; Vanoirbeek, J.; Himmelreich, U.; et al. Longitudinal micro-CT provides biomarkers of lung disease that can be used to assess the effect of therapy in preclinical mouse models, and reveal compensatory changes in lung volume. *Dis Model Mech.* **2016**, *9* (1), 91−8.

(10) Shofer, S.; Badea, C.; Qi, Y.; Potts, E.; Foster, W. M.; Johnson, G. A. A micro-CT analysis of murine lung recruitment in bleomycin-induced lung injury. *J. Appl. Physiol.* **2008**, *105* (2), 669−77.

(11) Scotton, C. J.; Hayes, B.; Alexander, R.; Datta, A.; Forty, E. J.; Mercer, P. F.; et al. Ex vivo micro-computed tomography analysis of bleomycin-induced lung fibrosis for preclinical drug evaluation. *Eur. Respir. J.* **2013**, *42* (6), 1633−45.

(12) Ruscitti, F.; Ravanetti, F.; Bertani, V.; Ragionieri, L.; Mecozzi, L.; Sverzellati, N.; et al. Quantification of Lung Fibrosis in IPF-Like Mouse Model and Pharmacological Response to Treatment by Micro-Computed Tomography. *Front. Pharmacol.* **2020**, *11*, 1.

(13) Mecozzi, L.; Mambrini, M.; Ruscitti, F.; Ferrini, E.; Ciccimarra, R.; Ravanetti, F.; et al. In-vivo lung fibrosis staging in a bleomycin-mouse model: a new micro-CT guided densitometric approach. *Sci. Rep.* **2020**, *10*, 10.

(14) Montesi, S. B.; Désogère, P.; Fuchs, B. C.; Caravan, P. Molecular imaging of fibrosis: recent advances and future directions. *J. Clin Invest.* **2019**, *129* (1), 24−33.

(15) Désogère, P.; Tapias, L. F.; Hariri, L. P.; Rotile, N. J.; Rietz, T. A.; Probst, C. K. Type I collagen-targeted PET probe for pulmonary fibrosis detection and staging in preclinical models. *Sci. Transl Med.* **2017**, *9* (384), 1.

(16) Désogère, P.; Tapias, L. F.; Rietz, T. A.; Rotile, N.; Blasi, F.; Day, H.; et al. Optimization of a Collagen-Targeted PET Probe for Molecular Imaging of Pulmonary Fibrosis. *J. Nucl. Med.* **2017**, *58* (12), 1991−6.

(17) Montesi, S. B.; Izquierdo-Garcia, D.; Désogère, P.; Abston, E.; Liang, L. L.; Digumarthy, S.; et al. Type I Collagen-targeted Positron Emission Tomography Imaging in Idiopathic Pulmonary Fibrosis: First-in-Human Studies. *Am. J. Respir Crit Care Med.* **2019**, *200* (2), 258−61.

(18) Bergmann, C.; Distler, J. H. W.; Treutlein, C.; Tascilar, K.; Müller, A. T.; Atzinger, A.; et al. 68Ga-FAPI-04 PET-CT for molecular assessment of fibroblast activation and risk evaluation in systemic sclerosis-associated interstitial lung disease: a single-centre, pilot study. *Lancet Rheumatology.* **2021**, *3* (3), e185−e194.

(19) Rosenkrans, Z. T.; Massey, C. F.; Bernau, K.; Ferreira, C. A.; Jeffery, J. J.; Schulte, J. J.; et al. [68Ga]Ga-FAPI-46 PET for noninvasive detection of pulmonary fibrosis disease activity. *European journal of nuclear medicine and molecular imaging.* **2022**, *49* (11), 3705.

(20) Yang, P.; Luo, Q.; Wang, X.; Fang, Q.; Fu, Z.; Li, J.; et al. Comprehensive Analysis of Fibroblast Activation Protein Expression in Interstitial Lung Diseases. *American Journal of Respiratory and Critical Care Medicine.* **2023**, *207* (2), 160−72.

(21) White, E. S.; Baralle, F. E.; Muro, A. F. New insights into form and function of fibronectin splice variants. *Journal of Pathology.* **2008**, *216* (1), 1−14.

(22) White, E. S.; Muro, A. F. Fibronectin splice variants: Understanding their multiple roles in health and disease using engineered mouse models. *IUBMB Life.* **2011**, *63* (7), 538−46.

(23) Bhattacharyya, S.; Tamaki, Z.; Wang, W.; Hinchcliff, M.; Hoover, P.; Getsios, S.; et al. FibronectinEDA Promotes Chronic Cutaneous Fibrosis Through Toll-like Receptor Signaling. *Sci. Transl Med.* **2014**, *6* (232), 232ra50.

(24) Klingberg, F.; Chau, G.; Walraven, M.; Boo, S.; Koehler, A.; Chow, M. L.; et al. The fibronectin ED-A domain enhances recruitment of latent TGF-β-binding protein-1 to the fibroblast matrix. *Journal of Cell Science [Internet].* **2018**, *131*, 131.

(25) Schwager, K.; Kaspar, M.; Bootz, F.; Marcolongo, R.; Paresce, E.; Neri, D.; et al. Preclinical characterization of DEKAVIL (F8-IL10), a novel clinical-stage immunocytokine which inhibits the progression of collagen-induced arthritis. *Arthritis Res. Ther.* **2009**, *11* (5), R142.

(26) McGaraughty, S.; Davis-Taber, R. A.; Zhu, C. Z.; Cole, T. B.; Nikkel, A. L.; Chhaya, M.; et al. Targeting Anti-TGF-β Therapy to Fibrotic Kidneys with a Dual Specificity Antibody Approach. *JASN.* **2017**, *28* (12), 3616−26.

(27) Sun, V. Z.; Melim, T. L.; Mitra, S.; Erickson, J. E.; Bryant, S. H.; Farnham, A.; et al. Fibronectin extra domain A as a drug delivery targeting epitope for rheumatoid arthritis. *Adv. Rheumatol.* **2022**, *62* (1), 17.

(28) Engebretsen, K. V.; Skårdal, K.; Bjørnstad, S.; Marstein, H. S.; Skrbic, B.; Sjaastad, I.; et al. Attenuated development of cardiac fibrosis in left ventricular pressure overload by SM16, an orally active inhibitor of ALK5. *Journal of molecular and cellular cardiology* **2014**, *76*, 148−57.

(29) Fu, K.; Corbley, M. J.; Sun, L.; Friedman, J. E.; Shan, F.; Papadatos, J. L.; et al. SM16, an orally active TGF-beta type I receptor inhibitor prevents myofibroblast induction and vascular fibrosis in the rat carotid injury model. *Arterioscler Thromb Vasc Biol.* **2008**, *28* (4), 665−71.

(30) Hübner, R. H.; Gitter, W.; Eddine El Mokhtari, N.; Mathiak, M.; Both, M.; Bolte, H.; et al. Standardized quantification of pulmonary fibrosis in histological samples. *BioTechniques.* **2008**, *44* (4), 507−17.

(31) Petersen, A. G.; Korntner, S. H.; Bousamaki, J.; Oró, D.; Arraut, A. M.; Pors, S. E.; Salinas, C. G.; et al. Reproducible lung protective effects of a TGFβR1/ALK5 inhibitor in a bleomycin-induced and spirometry-confirmed model of IPF in male mice. *Physiol Rep.* **2024**, *12* (19), No. e70077.

(32) Bonniaud, P.; Margetts, P. J.; Kolb, M.; Schroeder, J. A.; Kapoun, A. M.; Damm, D.; et al. Progressive transforming growth factor beta1-induced lung fibrosis is blocked by an orally active ALK5 kinase inhibitor. *Am. J. Respir Crit Care Med.* **2005**, *171* (8), 889−98.

(33) Zhang, L.; Wang, Y.; Homan, K. T.; Gaudette, S. M.; McCluskey, A. J.; Chan, Y.; et al. Imaging the Alternatively Spliced D Domain of Tenascin C in a Preclinical Model of Inflammatory Bowel Disease. *Mol. Imaging Biol.* **2023**, *25* (2), 314−23.

https://doi.org/10.1021/cbmi.4c00065
Chem. Biomed. Imaging 2025, 3, 85−94

(34) Peng, R.; Sridhar, S.; Tyagi, G.; Phillips, J. E.; Garrido, R.; Harris, P.; et al. Bleomycin Induces Molecular Changes Directly Relevant to Idiopathic Pulmonary Fibrosis: A Model for "Active" Disease. *PLoS One.* **2013**, *8* (4), No. e59348.
(35) Liu, T.; De Los Santos, F. G.; Phan, S. H. The Bleomycin Model of Pulmonary Fibrosis. In *Fibrosis: Methods and Protocols*; Methods in Molecular Biology; Rittié, L, Ed.; Springer: New York, NY; 2017; p 27−42; DOI: 10.1007/978-1-4939-7113-8_2.
(36) Izbicki, G.; Segel, M j.; Christensen, T g.; Conner, M w.; Breuer, R. Time course of bleomycin-induced lung fibrosis. *International Journal of Experimental Pathology.* **2002**, *83* (3), 111−9.
(37) Montgomery, M. K.; David, J.; Zhang, H.; Ram, S.; Deng, S.; Premkumar, V.; et al. Mouse lung automated segmentation tool for quantifying lung tumors after micro-computed tomography. *PLoS One* **2021**, *16* (6), No. e0252950.

https://doi.org/10.1021/cbmi.4c00065
Chem. Biomed. Imaging 2025, 3, 85−94